Bayesian Integration for Deep-Space Navigation with GNSS Signals

Bayesian Integration for Deep-Space Navigation with GNSS Signals

Oliviero Vouch, Andrea Nardin, Alex Minetto, Simone Zocca, Fabio Dovis
Department of Electronics and Telecommunications (DET), Politecnico di Torino, Torino, Italy
Lauren Konitzer, Joel J.K. Parker, Benjamin Ashman
NASA Goddard Space Flight Center, Greenbelt, Maryland, USA
Fabio Bernardi, Simone Tedesco, Samuele Fantinato
Qascom SRL, Bassano del Grappa, Vicenza, Italy

***Abstract*—Recent advancements in spaceborne receiver technology have extended the application of Global Navigation Satellite System (GNSS)-based navigation systems to space missions. However, the actual availability and usability of GNSS signals in deep-space is still questionable, lacking experimental evidence. The Lunar GNSS Receiver Experiment (LuGRE) is a joint NASA-Italian Space Agency (ASI) payload aiming to showcase GNSS-based Positioning, Navigation and Timing (PNT) during its transfer orbit to the Moon. Operating without direct interface with on-board Guidance, Navigation & Control (GNC) subsystems, the LuGRE receiver requires alternative means of aiding to pursue precise Orbit Determination (OD) in the challenging space environment. This paper investigates a custom Trajectory-Aware EKF (TA-EKF) architecture that integrates *aiding observations* in the form of a pre-mission design of the LuGRE trajectory. Two alternative designs are presented, integrating aiding observations in the observation-domain and state-domain, respectively. The proposed architectures are evaluated by post-processing raw GNSS observables collected in a real-time Hardware-in-the-Loop (HIL) simulation with GNSS Radio Frequency (RF) signals. A comprehensive assessment leveraging Monte Carlo (MC) analyses characterizes the OD performance under aiding observation errors and mismodeling, comparing the TA-EKF models against a standalone Extended Kalman Filter (EKF) solution.**

***Index Terms*—Satellite navigation systems, Navigation, Bayesian estimation, Kalman filters, Moon.**

I. Introduction

Nowadays, the navigation, guidance, and maneuvering of space vehicles predominantly rely on ground segment assets. The utilization of Radio Frequency (RF) tracking through Deep Space Networks (DSNs) facilities and Direct-to-Earth (DTE) links enables advanced Orbit Determination (OD) techniques that rely upon sophisticated off-board processing algorithms [1]. To afford semi-autonomous navigation, ground-based observations can be further combined with on-board relative measurements [2]. Similarly, maneuver control operations often involve telecommands from ground stations [3]. Ground-based assets have many advantages, but relying on them for OD and guidance introduces drawbacks. Operational costs escalate, and managing numerous missions can become impractical due to fast depletion of ground segment resources. Additionally, significant communication delays can hinder the success of latency-critical operations [4].

In light of the forthcoming deep-space exploration roadmap [5], there's an urgent need to enhance spacecraft autonomy to effectively address the challenges ahead. Within the Space Service Volume (SSV), Global Navigation Satellite Systems (GNSSs) are a fundamental asset for autonomous navigation. In fact, GNSS systems were conceived to supply Positioning, Navigation and Timing (PNT) services to terrestrial users, and their use has been recently foreseen and regulated up to high earth orbits and geosynchronous altitudes [6], [7]. However, the use of GNSS at higher altitudes faces significant hurdles. Earth obstruction of the satellite-to-spacecraft Line-of-Sight (LOS) largely (*i*) limits signal availability [8]. Moreover, even in good radiometric visibility conditions, (*ii*) the large pathloss accumulated by GNSS signals over deep-space distances results in weak signal reception and noisy observations. Yet (*iii*) multilateration solutions computed from such observations are affected by poor geometry caused by the unfortunate relative distribution of Earth-based satellites w.r.t. a user that is navigating the deep-space.

Despite the limitations mentioned above, interest has grown about using GNSS systems for autonomous navigation in transfer orbits (e.g., Earth-Moon transfer orbits (MTOs)) and for supporting propulsive maneuvers, such as trans-orbital injections or landings. [9]–[11]. Conforming to the dynamic OD approach, [12] combines filtered GNSS observations with predictions of the orbiting vehicle state based on a finely tuned orbital propagator . Moreover, the reduced dynamic OD approach additionally accounts for the uncertainties of fully dynamic trajectory modeling in the process noise, and [13] assessed this method for different filtering schemes using GPS data. Yet the navigation module can benefit from external a-priori information such as control inputs from Guidance, Navigation & Control (GNC) subsystems. Although approaches leveraging complex models of physical forces and orbital dynamics can afford highly accurate OD solutions, they have implications in terms of computational burden.

This study demonstrates the feasibility of onboard OD using

This study was funded within the contract n. 2021-26-HH.0 ASI/Politecnico di Torino "Attività di R&S inerente alla Navigazione GNSS nello Space volume Terra/Luna nell'ambito del Lunar GNSS Receiver Experiment". O. Vouch acknowledges funding from the Politecnico di Torino Interdepartmental Centre for Service Robotics (PIC4SeR). A. Minetto acknowledges funding from the research contract no. 32-G-13427-5 DM 1062/2021 funded within the Programma Operativo Nazionale (PON) Ricerca ed Innovazione of the Italian Ministry of University and Research (MUR).

GNSS observations without the need of real-time assistance from ground assets or external control data about vehicle dynamics. This operational assumption aligns with the design of the spaceborne GPS/Galileo dual-frequency receiver for the upcoming Lunar GNSS Receiver Experiment (LuGRE). LuGRE, a joint National Aeronautics and Space Administration (NASA)-Italian Space Agency (ASI) demonstration payload on the Firefly Blue Ghost Mission 1 (BGM1) lander, aims to showcase multi-GNSS-based PNT in cis-lunar space and at the Moon [14], [15]. The LuGRE receiver is designed to operate as a self-contained payload whose onboard OD can rely solely on GNSS observables and aiding data pre-loaded by the ground segment prior to mission deployment. One of the driving scientific objectives of LuGRE is to assess the performance of GNSS-based OD solutions obtained both onboard at mission time and through ground-based post-processing of multi-GNSS observables collected by the receiver in the MTO and on the Moon surface [16]–[18].

Building upon previous work [19], [20] targeting the kinematic approach to OD, this paper proposes an Extended Kalman Filter (EKF)-based architecture that integrates *aiding observations* in the form of a pre-mission design of the spacecraft trajectory. Two alternative Trajectory-Aware EKF (TA-EKF) algorithms are formulated, featuring *observation-domain* and *state-domain* integration of aiding observations, respectively. The former envisages aiding data integration in the measurement model, while the latter addresses flaws in the state prediction due to mismodeled motion dynamics. The developed TA-EKF architectures can enable autonomous GNSS-based orbital navigation aided with offline information about the dynamic system evolution, without the need to rely on external input controls from spacecraft GNC subsystems, and without real-time ground support. Additionally, the adoption of a simplistic model for state dynamics provides an attractive alternative to resource-intensive models of orbital motion.

Raw GNSS observables, as constructed by the LuGRE receiver from simulated RF signals relative to a MTO segment, are post-processed to showcase both TA-EKF models against a standalone EKF solution, demonstrating the limited orbital navigation performance achievable with the standalone approach. A comprehensive assessment of both aiding integration models is conducted through extensive Monte Carlo (MC) analyses to characterize OD performance under aiding observation errors and mismodeling.

II. Background

In the context of Bayesian inference as a statistical inversion problem, the Kalman Filter (KF) pursues optimal recursive regression for linear, Gaussian systems. For discrete-time systems involving non-linear transformations and possibly non-Gaussian statistics, the EKF undertakes a Gaussian approximation of the filtering distributions with Taylor series linearization of dynamic and observation models [21]. Assuming additive process and measurement noises, the EKF solution to the filtering problem reads as:

$$\boldsymbol{x}_k = \boldsymbol{f}_{k-1}(\boldsymbol{x}_{k-1}, \boldsymbol{c}_{d,k-1}) + \boldsymbol{w}_{k-1} \tag{1}$$

$$\boldsymbol{z}_k = \boldsymbol{h}_k(\boldsymbol{x}_k) + \boldsymbol{v}_k \tag{2}$$

where:

- $\boldsymbol{x}_k$ is the system state at time t_k.
- $\boldsymbol{z}_k$ is the measurement vector at time t_k.
- $\boldsymbol{w}_{k-1} \sim \mathcal{N}(\boldsymbol{0}, \boldsymbol{Q}_{k-1})$ and $\boldsymbol{v}_k \sim \mathcal{N}(\boldsymbol{0}, \boldsymbol{R}_k)$ are the zero-mean, normally distributed process and measurement noises with covariance matrices $\boldsymbol{Q}_{k-1}$ and $\boldsymbol{R}_k$, respectively.
- $\boldsymbol{f}_{k-1}$ and $\boldsymbol{h}_k$ are known state-transition and measurement functions, respectively.
- $\boldsymbol{c}_{d,k-1}$ are deterministic forcing inputs affecting the process state.

The estimation of the parameters of the Gaussian filtering distributions develops across a two-step procedure.

a) Prediction step:

$$\hat{\boldsymbol{x}}_k^- = \boldsymbol{f}_{k-1}(\hat{\boldsymbol{x}}_{k-1}) \tag{3}$$

$$\hat{\boldsymbol{P}}_k^- = \boldsymbol{\Phi}_{k-1}\hat{\boldsymbol{P}}_{k-1}\boldsymbol{\Phi}_{k-1}^T + \boldsymbol{Q}_{k-1} \tag{4}$$

where:

- $\hat{\boldsymbol{x}}_k^-$ is the a-priori state estimate at time t_k.
- $\hat{\boldsymbol{P}}_k^-$ is the a-priori state covariance estimate at time t_k.
- $\boldsymbol{\Phi}_{k-1}$ is the state transition matrix. For non-linear $\boldsymbol{f}_{k-1}$, it is the Jacobian matrix evaluated at $\hat{\boldsymbol{x}}_{k-1}$ (i.e., the latest a-posteriori state estimate).

b) Update step:

$$\boldsymbol{K}_k = \hat{\boldsymbol{P}}_k^- \boldsymbol{H}_k^T (\boldsymbol{H}_k \hat{\boldsymbol{P}}_k^- \boldsymbol{H}_k^T + \boldsymbol{R}_k)^{-1} \tag{5}$$

$$\hat{\boldsymbol{x}}_k = \hat{\boldsymbol{x}}_k^- + \boldsymbol{K}_k(\boldsymbol{z}_k - \boldsymbol{h}_k(\hat{\boldsymbol{x}}_k^-)) \tag{6}$$

$$\hat{\boldsymbol{P}}_k = \hat{\boldsymbol{P}}_k^- - \boldsymbol{K}_k \boldsymbol{H}_k \hat{\boldsymbol{P}}_k^- \tag{7}$$

where:

- $\hat{\boldsymbol{x}}_k$ is the a-posteriori state estimate at time t_k.
- $\hat{\boldsymbol{P}}_k$ is the a-posteriori state covariance estimate at time t_k.
- $\boldsymbol{H}_k$ is the measurement matrix. For non-linear $\boldsymbol{h}_k$, it is the Jacobian matrix evaluated at $\hat{\boldsymbol{x}}_k^-$.
- $\boldsymbol{K}_k$ is the Kalman gain matrix at time t_k.

A. System model for kinematic OD

In the context of the considered OD task based on GNSS signals, the system state is formulated as:

$$\boldsymbol{x}_k = \begin{bmatrix} \boldsymbol{r}_k & \dot{\boldsymbol{r}}_k & b_{u,k} & \dot{b}_{u,k} \end{bmatrix}^T \tag{8}$$

and it involves the following quantities:

- $\boldsymbol{r}_k = [r_{x,k}\, r_{y,k}\, r_{z,k}]$ the spacecraft absolute position vector expressed in Earth-Centered Inertial (ECI) coordinates;
- $\dot{\boldsymbol{r}}_k = [\dot{r}_{x,k}\, \dot{r}_{y,k}\, \dot{r}_{z,k}]$ the spacecraft absolute velocity vector expressed in ECI coordinates;
- $b_{u,k}$ the range equivalent of the GNSS receiver clock bias;
- $\dot{b}_{u,k}$ the range-rate equivalent of the GNSS receiver clock drift;

Under the assumption that the Gaussian filter is not subject to known control inputs reflecting process dynamics (i.e., $\boldsymbol{c}_{d,k-1} = \mathbf{0}$), a simplistic constant-velocity motion model is considered yielding the following state transition matrix:

$$\boldsymbol{\Phi}_{cv,k-1} = \begin{bmatrix} \boldsymbol{I}_{3\times3} & \boldsymbol{I}_{3\times3}\Delta t & \mathbf{0}_{3\times1} & \mathbf{0}_{3\times1} \\ \mathbf{0}_{3\times3} & \boldsymbol{I}_{3\times3} & \mathbf{0}_{3\times1} & \mathbf{0}_{3\times1} \\ \mathbf{0}_{1\times3} & \mathbf{0}_{1\times3} & 1 & \Delta t \\ \mathbf{0}_{1\times3} & \mathbf{0}_{1\times3} & 0 & 1 \end{bmatrix} \tag{9}$$

where Δt is the discrete-time state estimation interval, $\boldsymbol{I}_{n\times n}$ is the $n \times n$ identity matrix and $\mathbf{0}_{n\times n}$ is the $n \times n$ null-matrix. As a matter of fact, $\boldsymbol{\Phi}_{cv,k-1}$ obtained from discretization of continuous-time, linear differential equations; hence, the kinematic state model is not significantly affected by local linear approximations. Correspondingly, the process covariance matrix can be written with block-diagonal structure as:

$$\boldsymbol{Q}_{k-1} = \begin{bmatrix} \boldsymbol{Q}_p & \mathbf{0}_{6\times2} \\ \mathbf{0}_{2\times6} & \boldsymbol{Q}_t \end{bmatrix} \tag{10}$$

where $\boldsymbol{Q}_p$ is the component modelling the stochastics of the kinematic states in (8) and depends upon the driving acceleration noise density $\boldsymbol{S}_a$. $\boldsymbol{Q}_t$, instead, is the component for the timing states in (8) and depends upon S_t and S_f; the latter are the GNSS receiver clock phase drift and frequency drift, respectively[1]. More details about the dynamic model can be found in [20].

B. GNSS-based observation model

GNSS measurement functions for code-based ranging involve non-linear transformations. Given the processed signal from the i-th GNSS satellite visible at time t_k, the pseudorange measurement equation can be written in metric units as:

$$\rho_k^{s_i} = \|\boldsymbol{r}_k^{s_i} - \boldsymbol{r}_k\| + b_{u,k} + \epsilon_k^{s_i} \tag{11}$$

where $\|\cdot\|$ is the vector norm. In particular, the following quantities have been introduced:

- $\boldsymbol{r}_k^{s_i}$ the i-th GNSS satellite position vector at time t_k.
- $\epsilon_k^{s_i}$ is the nuisance term which aggregates all the errors in the pseudorange measurement for satellite i.

Differentiating (11) w.r.t. time, a pseudorange-rate measurement is extracted which is proportional to the Doppler-shift between the receiver and the i-th satellite. The pseudorange-rate equation takes the form:

$$\dot{\rho}_k^{s_i} = (\dot{\boldsymbol{r}}_k^{s_i} - \dot{\boldsymbol{r}}_k) \cdot \underbrace{\frac{\boldsymbol{r}_k^{s_i} - \boldsymbol{r}_k}{\|\boldsymbol{r}_k^{s_i} - \boldsymbol{r}_k\|}}_{\boldsymbol{u}_{r,k}^{s_i}} + \dot{b}_{u,k} + \dot{\epsilon}_k^{s_i} \tag{12}$$

where:

- $\dot{\boldsymbol{r}}_k^{s_i}$ the i-th GNSS satellite velocity at time t_K.
- $\dot{\epsilon}_k^{s_i}$ is the nuisance term which aggregates all the errors in the pseudorange-rate measurement for satellite i.
- $\boldsymbol{u}_{r,k}^{s_i}$ is the unit pointing vector from the receiver position to the i-th satellite position at time t_k.

[1]For $\boldsymbol{Q}_{k-1}$, $S_{c\phi} = 2.5 \cdot 10^{-12}\,(\text{m/s})^2/\text{Hz}$, $S_{cf} = 1.5 \cdot 10^{-4}\,(\text{m/s}^2)^2/\text{Hz}$, $S_{a,x} = S_{a,y} = S_{a,z} = 2\,(\text{m/s}^2)^2/\text{Hz}$ were set as in [22].

As a matter of fact, (12) is proportional to the radial component of the relative velocity between the satellite and the receiver.

Assuming m satellites signals being tracked at time t_k, the GNSS-based measurement vector can be formulated as:

$$\boldsymbol{z}_k^{GNSS} = \begin{bmatrix} \rho_k^{s_1} & \dots & \rho_k^{s_m} & \dot{\rho}_k^{s_1} & \dots & \dot{\rho}_k^{s_m} \end{bmatrix}^T . \tag{13}$$

Then, by applying first-order Taylor linearization of (11) and (12), it results the following measurement matrix for the GNSS-based observation model:

$$\boldsymbol{H}_k^{GNSS} = \begin{bmatrix} \boldsymbol{U}_{m\times3} & \mathbf{0}_{m\times3} & \mathbf{1}_{m\times1} & \mathbf{0}_{m\times1} \\ \mathbf{0}_{m\times3} & \boldsymbol{U}_{m\times3} & \mathbf{0}_{m\times1} & \mathbf{1}_{m\times1} \end{bmatrix} \tag{14}$$

where $\boldsymbol{U}_{m\times3}$ is the geometry matrix of pointing vectors to the m tracked satellites signals. Assuming the nuisance terms in (11) and (12) are i.i.d., the GNSS measurement noise covariance matrix $\boldsymbol{R}_k^{GNSS}$ is diagonal and the Carrier-to-Noise-density ratio (C/N_0) is taken as metric to estimate the component variances.

III. Methodology

Although ground-dependent tracking subsystems are the most conventional sources of aiding to the OD task, the proposed TA-EKF architectures are aided through an off-board, pre-mission design of the planned spacecraft orbit. The considered aiding observations, which correlate with the spacecraft's instantaneous kinematic state, can be originated from a high-precision orbit propagator. The latter can incorporate complex mathematical models accounting for gravitational effects from the Earth and other solar system bodies, atmospheric drag, solar radiation pressure, and other perturbations [23]. The following sections suggest two alternative strategies to profitably integrate aiding observations into the state-space model.

A. Observation-domain TA-EKF

Interpreting aiding observations as a known function of the spacecraft's state allows them to complement the GNSS-based observation set (13). Assuming additive measurement noise as in (2), the aiding measurement model for the EKF solution to the Bayesian filtering model would read as:

$$\tilde{\boldsymbol{z}}_k = \tilde{\boldsymbol{h}}_k(\boldsymbol{x}_k) + \boldsymbol{\zeta}_k \tag{15}$$

where:

- $\tilde{\boldsymbol{h}}_k$ is the known (and possibly non-linear) aiding measurement function.
- $\boldsymbol{\zeta}_k \sim \mathcal{N}\left(\mathbf{0}, \tilde{\boldsymbol{R}}_k\right)$ is the zero-mean, normally-distributed aiding measurement noise with covariance matrix $\tilde{\boldsymbol{R}}_k$.

Assuming $\tilde{\boldsymbol{h}}_k$ linear(-izable), (15) can be written in terms of the aiding measurement matrix:

$$\tilde{\boldsymbol{z}}_k = \tilde{\boldsymbol{H}}_k \boldsymbol{x}_k + \boldsymbol{\zeta}_k \ . \tag{16}$$

In this research, aiding observations are available as a pre-mission orbit plan which provides information about the spacecraft position and velocity states but not about the

GNSS receiver clock offset and drift states. Thus, the aiding measurement vector at time t_k is defined as:

$$\tilde{\boldsymbol{z}}_k = [\underbrace{\tilde{r}_{x,k}\, \tilde{r}_{y,k}\, \tilde{r}_{z,k}}_{\tilde{\boldsymbol{r}}_k}\ \underbrace{\tilde{\dot{r}}_{x,k}\, \tilde{\dot{r}}_{y,k}\, \tilde{\dot{r}}_{z,k}}_{\tilde{\dot{\boldsymbol{r}}}_k}]^T \tag{17}$$

where $\tilde{\boldsymbol{r}}_k$ and $\tilde{\dot{\boldsymbol{r}}}_k$ are, respectively, the position and velocity aiding states (i.e., spacecraft instantaneous kinematic states); hence, they admit a simple identity relationship with (8). It follows that the aiding measurement model is linear and the measurement equation yields the following aiding measurement matrix:

$$\tilde{\boldsymbol{H}}_k = \begin{bmatrix} \boldsymbol{I}_{6\times 6} & \boldsymbol{0}_{6\times 2} \end{bmatrix} \ . \tag{18}$$

In light of the foregoing, it is possible to define the composite measurement vector for the observation-domain TA-EKF:

$$\boldsymbol{z}_k = \begin{bmatrix} \boldsymbol{z}_k^{GNSS} & \tilde{\boldsymbol{z}}_k \end{bmatrix}^T \ . \tag{19}$$

Correspondingly, the composite measurement matrix for m satellites being processed at time t_k takes the form:

$$\boldsymbol{H}_k = \begin{bmatrix} \boldsymbol{H}_k^{GNSS} \\ \tilde{\boldsymbol{H}}_k \end{bmatrix} = \begin{bmatrix} \boldsymbol{U}_{m\times 3} & \boldsymbol{0}_{m\times 3} & \boldsymbol{1}_{m\times 1} & \boldsymbol{0}_{m\times 1} \\ \boldsymbol{0}_{m\times 3} & \boldsymbol{U}_{m\times 3} & \boldsymbol{0}_{m\times 1} & \boldsymbol{1}_{m\times 1} \\ \boldsymbol{1}_{3\times 3} & \boldsymbol{0}_{3\times 3} & \boldsymbol{0}_{3\times 1} & \boldsymbol{0}_{3\times 1} \\ \boldsymbol{0}_{3\times 3} & \boldsymbol{1}_{3\times 3} & \boldsymbol{0}_{3\times 1} & \boldsymbol{0}_{3\times 1} \end{bmatrix} \ . \tag{20}$$

The statistical modeling of aiding observations should align with the precision pursued by the external aiding source. As such, aiding observation weighting in $\tilde{\boldsymbol{R}}_k$ is expected to reflect the estimator's confidence in the aiding source. For the case at hand, variance weights are adjusted based on the accuracy of the physics-based models integrated into the orbit design and maneuver planning software [23]. Alternatively, $\tilde{\boldsymbol{R}}_k$ might be designed based on pre-mission requirements allocated to the external aiding source. Moreover, statistical independence between GNSS measurements and aiding observations can be safely assumed when the latter result from a pre-mission orbital planning. It follows a block-diagonal measurement noise covariance in the observation-domain TA-EKF:

$$\boldsymbol{R}_k = \begin{bmatrix} \boldsymbol{R}_k^{GNSS} & \boldsymbol{0}_{m\times 6} \\ \boldsymbol{0}_{6\times m} & \tilde{\boldsymbol{R}}_k \end{bmatrix} \ . \tag{21}$$

B. State-domain TA-EKF

The EKF solution to the mean of the predictive state distribution (3) might suffer from large errors due to misspecified orbital dynamics in the overly simple motion model (9). In turns, this would enhance the local linearization errors of the GNSS measurement functions according to Section II-B. Avoiding to resort to more complex dynamic models and in absence of prior information about the system state evolution from external controls, aiding observations can be integrated in the dynamic model to enhance the accuracy of the a-priori state estimate.

Based on these premises, the state-domain TA-EKF design pursues an optimal weighted estimate of the Gaussian predictive state distribution by combining two a-priori estimates of the unknown state:

- the time-propagated estimate yielded by the constant-velocity kinematic state model (9);
- an *aiding state* $\tilde{\boldsymbol{x}}_k$ yielded by the aiding measurement model (15).

At time t_k, the time-propagated estimate and the associated estimation error covariance can be obtained as:

$$\hat{\boldsymbol{x}}_{cv,k} = \boldsymbol{\Phi}_{cv,k-1}\hat{\boldsymbol{x}}_{k-1} \tag{22}$$

$$\hat{\boldsymbol{P}}_{cv,k} = \boldsymbol{\Phi}_{cv,k-1}\hat{\boldsymbol{P}}_{k-1}\boldsymbol{\Phi}_{cv,k-1}^T + \boldsymbol{Q}_{k-1} \ . \tag{23}$$

Concerning the aiding state and its covariance, a Weighted Least-Squares (WLS) estimate can be obtained from the linear(-ized) aiding measurement model (16) as:

$$\tilde{\boldsymbol{x}}_k = \left(\tilde{\boldsymbol{H}}_k^\top \tilde{\boldsymbol{R}}_k^{-1}\tilde{\boldsymbol{H}}_k\right)^{-1} \tilde{\boldsymbol{H}}_k^\top \tilde{\boldsymbol{R}}_k^{-1}\tilde{\boldsymbol{z}}_k \tag{24}$$

$$\tilde{\boldsymbol{P}}_k = \left(\tilde{\boldsymbol{H}}_k^\top \tilde{\boldsymbol{R}}_k^{-1}\tilde{\boldsymbol{H}}_k\right)^{-1} \tag{25}$$

where (25) propagates the aiding covariance $\tilde{\boldsymbol{R}}_k$ in the aiding state. The existence of both (24) and (25) is tied to the application context and the nature of the aiding, and thus should be properly evaluated on a case-by-case basis. In the present study, $\tilde{\boldsymbol{x}}_k$ straightly matches the aiding measurement vector (17) at time t_k, and the relation $\tilde{\boldsymbol{P}}_k = \tilde{\boldsymbol{R}}_k$ holds.

State-domain integration leverages the assumption that both a-priori point estimates are realizations of multivariate Gaussian random variables with matching mode—the true yet unknown system state—and different covariance matrices. An optimal estimate of the mean of the predictive state distribution is obtained by Generalized Least-Squares (GLS). The following quadratic loss can be defined:

$$L(\boldsymbol{x}_{k,\mathrm{est}}; \boldsymbol{x}_k, \hat{\boldsymbol{P}}_{cv,k}, \tilde{\boldsymbol{P}}_k) = \Delta\boldsymbol{x}_k^T(\hat{\boldsymbol{P}}_{cv,k}^{-1} + \tilde{\boldsymbol{P}}_k^{-1})\Delta\boldsymbol{x}_k \tag{26}$$

where $\Delta\boldsymbol{x}_k = \boldsymbol{x}_{k,\mathrm{est}} - \boldsymbol{x}_k$ and $\boldsymbol{x}_{k,\mathrm{est}}$ is the estimate of $\boldsymbol{x}_k$ considered to evaluate the loss. As a matter of fact, (26) evaluates the Mahalanobis length of the residual between the estimate and the true system state. The a-priori state estimate at time t_k for the state-domain TA-EKF is the Minimum-Mean-Square Error (MMSE) estimate:

$$\hat{\boldsymbol{x}}_k^- = (\hat{\boldsymbol{P}}_{cv,k}^{-1} + \tilde{\boldsymbol{P}}_k^{-1})^{-1}(\hat{\boldsymbol{P}}_{cv,k}^{-1}\boldsymbol{\Phi}_{cv,k-1}\hat{\boldsymbol{x}}_{k-1} + \tilde{\boldsymbol{P}}_k^{-1}\tilde{\boldsymbol{x}}_k) \tag{27}$$

which turns out being the Best Linear Unbiased estimator (BLUE) for the loss (26) [24]. The a-priori estimation error covariance estimate is retrieved by resorting to the uncertainty propagation principle for linear combinations [25]:

$$\hat{\boldsymbol{P}}_k^- = (\hat{\boldsymbol{P}}_{cv,k}^{-1} + \tilde{\boldsymbol{P}}_k^{-1})^{-1} \tag{28}$$

with statistical independence between $\hat{\boldsymbol{x}}_{cv,k}$ and $\tilde{\boldsymbol{x}}_k$ being assumed.

IV. Experimental testbed

Taking the LuGRE mission as case-study of GNSS-based PNT in MTO, a simulation-based analysis with representative RF signals and Hardware-in-the-Loop (HIL) is carried out relative to a segment of the LuGRE orbit at 17 Earth Radii (RE).

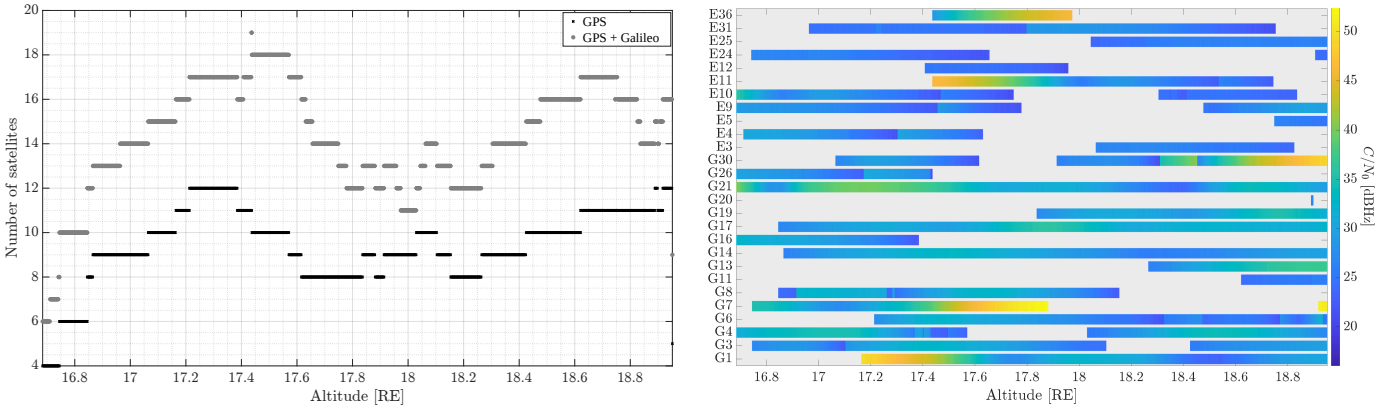

(a) Radiometric visibility of GNSS satellites

(b) C/N_0 profile

Fig. 1. GNSS operational environment along the analyzed segment of LuGRE MTO.

A. Radio-frequency simulation scenario

A multi-GNSS simulation model is configured in Spirent GSS9000 GNSS RF simulator [26] to emulate the dynamic environment and the GNSS signal conditions the LuGRE payload is expected to be subject to in deep-space. Taking a pre-mission trajectory design as reference model of the space vehicle orbit, GPS and Galileo satellite positions are reproduced from precise ephemeris and interpolated to cover a 2 hours long simulation span. Space-weather effects and ephemeris errors are considered for their impact on GNSS signals to enhance the realism of the test scenario. A HIL test is then set-up by integrating the GNSS receiver described in Section IV-B in the simulation testbench. Specifically, digital GNSS signals samples are created by Spirent SimGEN control software for GPS L1/L5 and Galileo E1/E5 bands, before being converted to analogue RF signals processed by the receiver front-end. According to the signal acquisition and tracking sensitivity of the receiver, Figure 1a shows the expected visibility of GNSS satellites for both constellations over the whole simulation span. Moreover, the estimated C/N_0 profile is highlighted in Figure 1b for the received GPS (G) and Galileo (E) satellite signals. The multi-GNSS raw observables obtained by the real-time operation of the radio receiver are logged, and the developed TA-EKF models are run in post-processing on the retrieved dataset.

B. Spaceborne GNSS receiver

The HIL simulation integrates a Moon-customized development of the Qascom QN400-SPACE [27], a dual-constellation and dual-band GNSS Software Defined Radio (SDR) receiver tailored to operate in deep-space in the context of LuGRE. This receiver plays a pivotal role in the acquisition and processing of simulated RF satellite signals, thereby constituting the backbone of the raw GNSS observables collection. The QN400-SPACE employs both coherent and non-coherent signal acquisition schemes to mitigate the challenges posed by weak GNSS signal power in deep space navigation. The acquisition process involves two stages: initially, satellites with the highest received power are acquired using a larger search space in the domain. Then, signals at lower power are acquired, reducing Doppler space by estimating clock drift. Signal tracking refines signal frequency and code phase estimates, demodulates navigation data, and generates GNSS raw measurements. The receiver's tracking loop performance is fine-tuned through semi-analytical analysis and MC simulations, resulting in improved signal tracking lock success rates, especially in noisy environments. This optimization process significantly enhances receiver robustness and performance.

C. Stochastic model of aiding observations

Aiding observations of discrete-time kinematics are synthetically constructed starting from the pre-mission design of the planned spacecraft orbit. Then, aiding observations are corrupted with a time-variant bias component driven by additive white noise. This approach is meant to model expected discrepancies between the aiding observations and the GNSS measurements. In particular, a temporal mismatch (i.e., a time offset) can set under asynchronous aiding data integration. In a real application, aiding observations are supplied to the PNT module as a sequence of space vehicle kinematic states at equi-spaced points in time. As soon as a new set of raw GNSS observables is available to the receiver, a synchronous sample from the aiding sequence must be selected. However, aiding observations are likely to be timestamped to a time-scale different from the one of the GNSS receiver [28]. Moreover, the rate of the aiding sequence can be different from the Position, Velocity, Timing (PVT) rate. Although the proposed method can bear limited mismatch as shown in Section V, the optimal selection of the aiding observation sample can be addressed resorting to preprocessing methods [29] which are beyond the scope of this work.

In the experimental analysis, the aiding measurement vector at time t_k is formulated as:

$$\tilde{\boldsymbol{z}}_k = \left[\tilde{\boldsymbol{r}}_k \; \tilde{\dot{\boldsymbol{r}}}_k\right]^T + \tilde{\boldsymbol{b}}_k \tag{29}$$

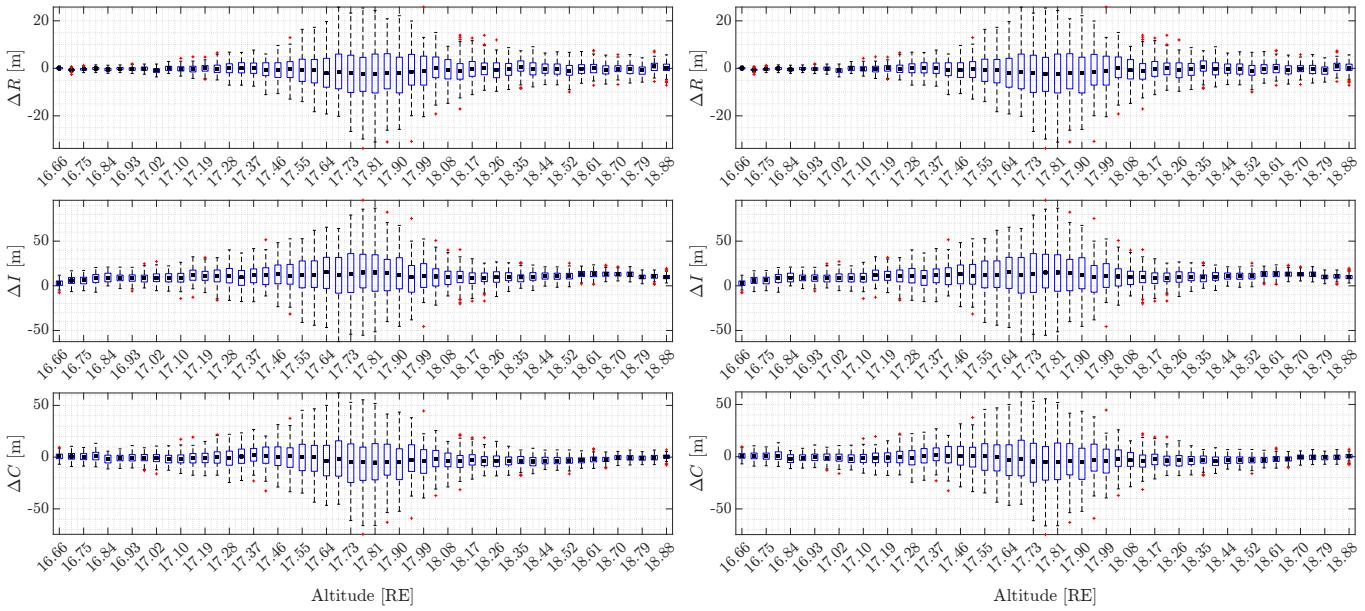

(a) observation-domain TA-EKF

(b) state-domain TA-EKF

Fig. 2. Statistical characterization of the OD solution in RIC frame for the TA-EKF models. Horizontal altitude ticks (in RE) are referred to the simulated segment of the LuGRE MTO.

where the first term embeds the spacecraft kinematic state from the planned spacecraft orbit and $\tilde{\boldsymbol{b}}_k$ is the introduced aiding bias factor. This bias is simulated as a discrete-time sequence of samples drawn from a multiple, first-order autoregressive AR(1) model [25]:

$$\tilde{\boldsymbol{b}}_k - \boldsymbol{m}_b = \boldsymbol{A}_k \left(\tilde{\boldsymbol{b}}_{k-1} - \boldsymbol{m}_b \right) + \boldsymbol{\eta}_k \tag{30}$$

where the time-variant matrix of first-order coefficients is defined based on the spacecraft velocity and acceleration states:

$$\boldsymbol{A}_k = \begin{bmatrix} \tilde{\dot{\boldsymbol{r}}}_k / \|\tilde{\dot{\boldsymbol{r}}}_k\| & \boldsymbol{0}_{3\times3} \\ \boldsymbol{0}_{3\times3} & \tilde{\ddot{\boldsymbol{r}}}_k / \|\tilde{\ddot{\boldsymbol{r}}}_k\| \end{bmatrix} . \tag{31}$$

The mean values of each component bias time-series impairing the aiding spacecraft kinematic state are collected in $\boldsymbol{m}_b$. Eventually, $\boldsymbol{\eta}_k$ is the zero-mean, normally distributed driving noise term with steady-state covariance $\tilde{\boldsymbol{\Sigma}}_k$. Expanding upon the asynchronous mismatching behavior captured by the AR(1) process, the driving noise term allows to account for residual unmodeled effects (e.g., unpredicted thrusting maneuvers).

V. Results

Based on the experimental framework presented in Section IV, the OD solutions from the TA-EKF models are analyzed when filtering in post-processing the GNSS observations as provided by the QN-400 SPACE receiver, and navigation accuracy performance is highlighted against the reference spacecraft orbit. In particular, for the simulated segment of LuGRE MTO, a sample of 10^3 MC realizations of the AR(1) bias process is collected to significantly characterize the error statistics of the aided navigation solutions. For each

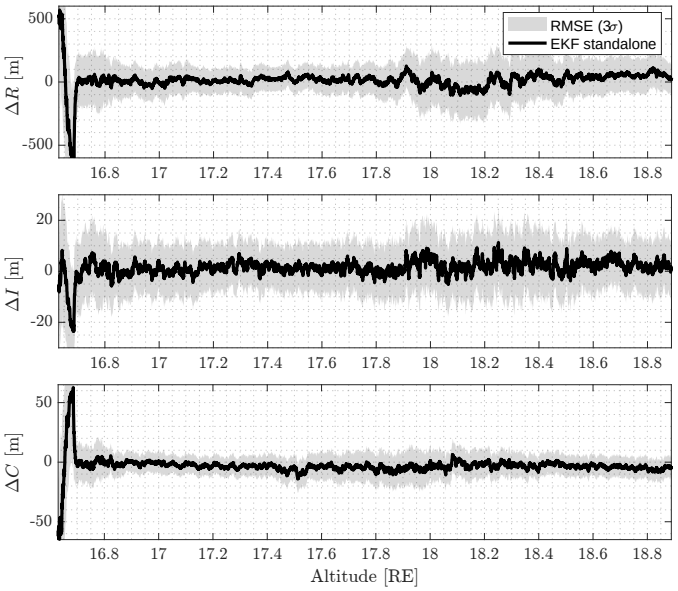

Fig. 3. Standalone EKF OD error in RIC coordinates with 3-sigma confidence intervals from the square-root of the corresponding diagonal elements in $\hat{\boldsymbol{P}}_k$.

MC realization, the mean value of each component bias time-series in (30) is drawn as a probabilistic outcome:

$$\boldsymbol{m}_b \sim \mathcal{N}\left(\boldsymbol{0}_{6\times1}, \begin{bmatrix} \sigma_p^2 \boldsymbol{I}_{3\times3} & \boldsymbol{0}_{3\times3} \\ \boldsymbol{0}_{3\times3} & \sigma_v^2 \boldsymbol{I}_{3\times3} \end{bmatrix} \right) \tag{32}$$

where $\sigma_p = 5$ m and $\sigma_v = 0.1$ m/s. To highlight the benefit of integrating aiding observations, a GNSS-based kinematic OD via a standalone EKF is included as benchmark to quantify the accuracy enhancement pursued by the proposed TA-EKF

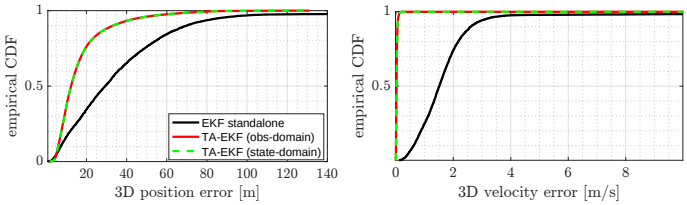

(a) Position (b) Velocity

Fig. 4. Position (left) and velocity (right) cumulative error statistics for both the standalone EKF and the TA-EKF architectures.

models. Yet filtering-based post-processing of combined GPS-Galileo observables (GPS L1/L5 - Galileo E1/E5) implementing dual-frequency iono-free linear combination is examined for all the involved EKF-based architectures.

Accuracy and precision of the OD solution are characterized in Figure 2, where the time-series of position estimation error are illustrated in Radial, In-track, Cross-track (RIC) frame for both observation-domain TA-EKF (Figure 2a) and state-domain TA-EKF (Figure 2b). In each spatial coordinate, errors are calculated against the reference spacecraft orbit and are regularly observed at different altitudes over the whole orbital segment. Each box represents the summary positioning error statics as the instantaneous output of the collected MC sample from 10^3 realizations of the AR(1) bias process. The top and bottom edges of the box (i.e., the interquartile range) indicate the 75-th and 25-th percentiles, respectively, and the black mark with a square shape inside the interquartile range identifies the mean of the MC sample. The lines extending above and below each box are referred to as whiskers. The latter goes from the end of the interquartile range to the furthest MC realization within the whisker length. Observations beyond the whisker length are marked as outliers and are relevant to characterizing the instantaneous position estimation uncertainty. As a matter of fact, the TA-EKF solutions demonstrate equivalent performance. In fact, when both (24) and (25) exist, the state-domain model adheres to the alternative information filter formulation [30]. This outcome is valuable as it ensures the flexibility to select the most convenient architecture based on the application context and the nature of the aiding observations.

The time-series of position estimation error in RIC components when filtering multi-GNSS observations with a standalone EKF are depicted in Figure 3. In each subplot, the individual error time-series are shown with black, solid lines, and the outer boundaries of the gray, shaded areas highlight the Root-Mean-Square Error (RMSE) measured at 3-sigma. Moreover, Fig. 4 illustrates the empirical Cumulative Density Function (CDF) lines in terms of 3D position (top) and velocity (bottom) estimation errors. In addition, summary cumulative error statistics at relevant percentiles are listed in Table I for the 3D position estimate and in Table II for the 3D velocity estimate. For the position estimate, the accuracy improvement pursued by the TA-EKFs as measured at the 50-th percentile amounts to 58.12%, while at the 95-th percentile it equals to 47.16%. For the velocity estimate,

TABLE I
CUMULATIVE POSITION ERROR STATISTICS (IN [m]) FOR TA-EKF ARCHITECTURES AND THE STANDALONE EKF.

Navigation Filter	CDF (percentile)			
	25	50	75	95
EKF standalone	14.78	29.409	48.884	86.230
TA-EKF (observation-domain)	8.259	12.316	19.431	45.568
TA-EKF (state-domain)	8.259	12.316	19.431	45.568

TABLE II
CUMULATIVE VELOCITY ERROR STATISTICS (IN [m/s]) FOR TA-EKF ARCHITECTURES AND THE STANDALONE EKF.

Navigation Filter	CDF (percentile)			
	25	50	75	95
EKF standalone	1.002	1.510	2.025	3.114
TA-EKF (observation-domain)	0.015	0.023	0.037	0.077
TA-EKF (state-domain)	0.015	0.023	0.037	0.077

instead, the 50-th percentile and 95-th percentile estimation accuracy improvements are 98.48% and 97.53%, respectively.

For the standalone EKF, the vulnerability of a kinematic approach to OD is evident. This filtering architecture propagates the spacecraft kinematic state between successive position fixing epochs through simplistic model-based dynamics, and the Kalman gain weigh much GNSS observations to sequentially update the orbit estimate. However, the space environment at high-altitudes emphasizes non-systematic errors in pseudorange observables due to weak received signal conditions (i.e., high receiver noise). Moreover, the spatial distribution of satellites exacerbates the propagation of pseudorange noise over the computed orbit solution. Nevertheless, systematic errors may arise in such extreme conditions as well. Established corrective models, widely adopted for terrestrial applications, might be out of their validity domain in deep space. Being pushed outside of their nominal working point, the use and effects of such models in the experimental setup are still under investigation. Nonetheless, these effects can be successfully mitigated via the TA-EKF solutions, even under circumstances of mild asynchrony between GNSS measurements and aiding observations as modelled by the AR(1) bias process, thus emphasizing the proposed techniques' robustness.

VI. CONCLUSION

This paper has addressed the task of autonomous OD based on GNSS signals for high-altitude space applications. Adhering to the kinematic OD approach, which is free from assumptions about process dynamics, a TA-EKF model has been proposed to pursue meter-level GNSS-based navigation of an orbiting vehicle. This is accomplished by leveraging on aiding data consisting of kinematic observations of the spacecraft trajectory as retrieved from a pre-launch orbit design. Two alternative yet equivalent TA-EKF models are foreseen. The observation-domain TA-EKF expands the filter measurement

model by complementing GNSS measurements with the observations of the spacecraft kinematic state. The state-domain TA-EKF, instead, improves the filter prediction by optimally weighting the time-propagated state with the kinematic aiding observations. The developed filtering architectures are assessed in the framework of LuGRE, a joint NASA/ASI demonstration payload which will fly a GPS/Galileo receiver expected to process real GNSS signals in transit between Earth and the Moon, in lunar orbit, and on the lunar surface. For a segment of the LuGRE MTO, HIL dual-constellation, dual-frequency observations are collected through a Spirent simulation and post-processed via the aided filters. Results highlight equivalent OD performance for the aided estimator architectures, thus allowing the flexibility to choose the most affordable, well-defined model depending on the characteristics of the aiding data. Extensive MC analyses are simulated to draw significant performance statistics when mild discrepancies between GNSS measurements and aiding data are taken into account, ans meter-level OD accuracy is demonstrated. Compared to a standalone EKF architecture, the position and velocity estimation accuracies can be enhanced up to 47.16% and 97.53% at the 95-th percentile, respectively. Recognizing the pitfalls of asynchronous aiding data integration, further effort will be devoted to calibration techniques that can handle the alignment between aiding observations and GNSS measurements. Yet a finer non-linear model reflecting orbital dynamics is about to be tested jointly with the integration of aiding data.

REFERENCES

[1] L. Iess, M. Di Benedetto, N. James, M. Mercolino, L. Simone, and P. Tortora, "Astra: Interdisciplinary study on enhancement of the end-to-end accuracy for spacecraft tracking techniques," *Acta Astronautica*, vol. 94, no. 2, pp. 699–707, 2014.

[2] E. Turan, S. Speretta, and E. Gill, "Performance analysis of crosslink radiometric measurement based autonomous orbit determination for cislunar small satellite formations," *Advances in Space Research*, 2022.

[3] S. K. Biswas and H. B. Hablani, "Ground based navigation of spacecraft in lunar transfer trajectory, with application to chandrayaan-2," in *Advances in Estimation, Navigation, and Spacecraft Control*, D. Choukroun, Y. Oshman, J. Thienel, and M. Idan, Eds. Berlin, Heidelberg: Springer Berlin Heidelberg, 2015, pp. 371–390.

[4] E. Turan, S. Speretta, and E. Gill, "Autonomous navigation for deep space small satellites: Scientific and technological advances," *Acta Astronautica*, vol. 193, pp. 56–74, 2022.

[5] International Space Exploration Coordination Group (ISECG), "The Global Exploration Roadmap. Technical report, International Space Exploration Coordination Group (ISECG)," ISECG, Tech. Rep., 2018.

[6] J. J. Parker, F. H. Bauer, B. W. Ashman, J. J. Miller, W. Enderle, and D. Blonski, "Development of an interoperable gnss space service volume," in *Proceedings of the 31st International Technical Meeting of the Satellite Division of The Institute of Navigation (ION GNSS+ 2018)*, 2018, pp. 1246–1256.

[7] United Nations Office for Outer Space Affairs, "The interoperable global navigation satellite systems space service volume," *United Nations Digital Library*, pp. vii, 96 p. :, Oct 2018.

[8] V. Capuano, C. Botteron, J. Leclère, J. Tian, Y. Wang, and P.-A. Farine, "Feasibility study of GNSS as navigation system to reach the Moon," *Acta Astronautica*, vol. 116, pp. 186–201, 2015.

[9] J. L. Burch, T. E. Moore, R. B. Torbert, and B. L. Giles, "Magnetospheric Multiscale Overview and Science Objectives," *Space Science Reviews*, vol. 199, no. 1, pp. 5–21, Mar. 2016.

[10] D. Baird, "Record-breaking satellite advances NASA's exploration of high-altitude GPS," *www.nasa.gov*, 2019, Accessed on: Nov. 23, 2022.

[11] L. Musumeci, F. Dovis, J. S. Silva, P. F. da Silva, and H. D. Lopes, "Design of a High Sensitivity GNSS receiver for Lunar missions," *Advances in Space Research*, vol. 57, no. 11, pp. 2285–2313, Jun. 2016.

[12] V. Capuano, "GNSS-based Orbital Filter for Earth Moon Transfer Orbits," *Journal of Navigation*, 10 2015.

[13] O. Montenbruck, T. Van Helleputte, R. Kroes, and E. Gill, "Reduced dynamic orbit determination using gps code and carrier measurements," *Aerospace Science and Technology*, vol. 9, no. 3, pp. 261–271, 2005.

[14] J. J. Parker, F. Dovis, B. Anderson, L. Ansalone, B. Ashman, F. H. Bauer, G. D'Amore, C. Facchinetti, S. Fantinato, G. Impresario *et al.*, "The Lunar GNSS Receiver Experiment (LuGRE)," in *Proceedings of the 2022 International Technical Meeting of The Institute of Navigation (ION ITM 2022)*, 2022, pp. 420–437.

[15] L. Konitzer, N. Esantsi, and J. Parker, "Navigation Performance Analysis and Trades for the Lunar GNSS Receiver Experiment (LuGRE)," in *2022 AAS/AIAA Astrodynamics Specialist Conference*, 8 2022.

[16] A. Minetto, F. Dovis, A. Nardin, O. Vouch, G. Impresario, and M. Musmeci, "Analysis of GNSS data at the Moon for the LuGRE project," in *2022 IEEE 9th International Workshop on Metrology for AeroSpace (MetroAeroSpace)*, Jun. 2022, pp. 134–139, iSSN: 2575-7490.

[17] A. Nardin, A. Minetto, O. Vouch, M. Maiani, and F. Dovis, "Snapshot acquisition of GNSS signals in space: a case study at lunar distances," in *Proceedings of the 35th International Technical Meeting of the Satellite Division of The Institute of Navigation (ION GNSS+ 2022)*, Denver, Colorado, September 2022, pp. 3603 – 3617.

[18] A. Nardin, A. Minetto, S. Guzzi, F. Dovis, L. Konitzer, and J. J. K. Parker, "Snapshot tracking of GNSS signals in space: A case study at lunar distances," in *Proceedings of the 36th International Technical Meeting of the Satellite Division of The Institute of Navigation (ION GNSS+ 2023)*, Denver, Colorado, September 2023, pp. 3267–3281.

[19] O. Vouch, A. Nardin, A. Minetto, M. Valvano, S. Zocca, and F. Dovis, "A customized EKF model for GNSS-based navigation in the harsh space environment," in *2023 IEEE International Conference on Wireless for Space and Extreme Environments (WiSEE)*, 2023, pp. 13–18.

[20] O. Vouch, A. Nardin, A. Minetto, S. Zocca, M. Valvano, and F. Dovis, "Aided kalman filter models for gnss-based space navigation," *IEEE Journal of Radio Frequency Identification*, pp. 1–1, 2024.

[21] S. Särkkä and L. Svensson, *Bayesian filtering and smoothing*. Cambridge university press, 2023, vol. 17.

[22] R. G. Brown and P. Y. Hwang, "Introduction to random signals and applied kalman filtering(book)," *New York, John Wiley & Sons, Inc., 1992. 512*, 1992.

[23] D. A. Vallado, R. S. Hujsak, T. M. Johnson, J. H. Seago, and J. W. Woodburn, "Orbit determination using odtk version 6," *Proceedings of the European Space Astronomy Centre, Madrid, Spain*, pp. 3–6, 2010.

[24] W.-L. Loh, "Estimating the common mean of two multivariate normal distributions," *The Annals of Statistics*, vol. 19, no. 1, pp. 297–313, 1991.

[25] S. M. Kay, *Fundamentals of statistical signal processing: estimation theory*. USA: Prentice-Hall, Inc., 1993.

[26] Spirent, "GSS9000 GNSS Simulator," Spirent Communications, Crawley, UK.

[27] S. Tedesco, F. Bernardi, S. Guzzi, M. Boschiero, M. Pulliero, D. Marcantonio, M. Ghedin, E. Miotti, S. Fantinato, O. Pozzobon, C. Facchinetti, M. Musmeci, G. D'Amore, G. Varacalli, A. Minetto, F. Dovis, J. J. K. Parker, S. A. McKim, L. Konitzer, B. Ashman, S. Sanathanamurthy, J. J. Miller, L. Valencia, and F. Bauer, "Deep space gnss in moon transfer orbit: the lugre receiver," in *2023 IEEE International Conference on Wireless for Space and Extreme Environments (WiSEE)*, 2023, pp. 1–6.

[28] Y. Guo, O. Vouch, S. Zocca, A. Minetto, and F. Dovis, "Enhanced EKF-Based Time Calibration for GNSS/UWB Tight Integration," *IEEE Sensors Journal*, vol. 23, no. 1, pp. 552–566, 2023.

[29] B.-K. Yi, H. Jagadish, and C. Faloutsos, "Efficient retrieval of similar time sequences under time warping," in *Proceedings 14th International Conference on Data Engineering*, 1998, pp. 201–208.

[30] Y. Bar-Shalom, X. R. Li, and T. Kirubarajan, *Estimation with applications to tracking and navigation: theory algorithms and software*. John Wiley & Sons, 2004.